Implementation and comparison of three isogeometric Navier-Stokes solvers applied to simulation of flow past a fixed 2D NACA0012 airfoil at high Reynolds number

Knut Nordanger[a,*], Runar Holdahl[b], Arne Morten Kvarving[b], Adil Rasheed[b], Trond Kvamsdal[a,b]

[a]*Department of Mathematical Sciences, Norwegian University of Science and Technology, NO-7491 Trondheim, Norway*
[b]*SINTEF ICT, Department of Applied Mathematics, Postboks 4760 Sluppen, NO-7465 Trondheim, Norway*

Abstract

Implementation of three different Navier-Stokes solvers in an isogeometric finite element framework is presented in this paper. The three solvers *Chorin projection method* and *Coupled formulation*, both with the Spalart–Allmaras turbulence model, and *Variational Multiscale (VMS) method* have been applied to simulate flow past a two-dimensional NACA0012 airfoil at a high Reynolds number ($Re = 3 \times 10^6$) for four different angles of attack. The predicted flow characteristics have been compared and the effects of increasing the order of the spline element on the accuracy of prediction and computational efficiency is evaluated. In this study it turns out that flow separation does not take place up to an angle of attack of $16°$. Up to this angle of attack all three solvers predict similar results in good agreement with each other and with available experimental results. However, a big spread in lift and drag coefficients is observed in the stall regime. Our study also shows that for linear spline elements all three solvers are computationally similar. For quadratic spline elements the Chorin solver compares favorably to the others based on the results presented here.

Keywords: Isogeometric analysis, NACA0012 airfoil, Chorin projection method, Spalart-Allmaras, Variational Multiscale

1. Introduction

Renewable energy is a growing sector with promising prospects of generating energy from wind as an important driving force. Therefore, being able to simulate flow around wind turbines is becoming increasingly important as the demand for larger and larger offshore wind turbines is growing. Larger turbines present many new challenges which cannot easily be addressed by traditional engineering methods.

---

*Corresponding author
    Email addresses:* `knut.nordanger@math.ntnu.no` (Knut Nordanger),
`runar.holdahl@sintef.no` (Runar Holdahl), `arne.morten.kvarving@sintef.no` (Arne Morten Kvarving), `adil.rasheed@sintef.no` (Adil Rasheed), `trond.kvamsdal@math.ntnu.no` (Trond Kvamsdal)

Many methods exist for computing flow around wind turbines. Today an increased focus is put on the overall simulation efficiency, i.e. the time consumption related to modelling, analysis and interpretation of results. In particular, the lack of interoperability between modelling using modern Computer Aided Design (CAD) systems and classical finite element analysis programs is a bottleneck. To address this bottleneck the concept of isogeometric analysis was introduced by Thomas J. R. Hughes and co-workers [1, 2]. This concept is characterized by using splines, i.e. B-splines or non-rational uniform B-splines (NURBS), as basis functions in the finite element analysis as well as in the CAD system. In turn, this opens up for exact geometric modelling, which can be of utmost importance when it comes to modelling aerodynamically shaped objects like airfoils. Furthermore, isogeometric analysis gives better accuracy per degree-of-freedom than more traditional methods.

The computational efficiency of isogeometric analysis methods for solving the incompressible Navier-Stokes equations is a current research topic. Aiming at attaining a solution as quickly as possible within a desired, acceptable accuracy is an obvious goal in all design situations. The pioneers in isogeometric analysis, such as Yuri Bazilevs among others, have developed coupled formulations based on variational multiscale stabilization (VMS) [3] and VMS turbulence models based on the work by Victor Calo [4]. These models have been further developed in [5].

Designing efficient linear solvers for fully coupled formulations of the incompressible Navier-Stokes flows as mentioned above is very challenging because of the coupling of the velocity and pressure unknowns through the incompressibility constraint. Projection methods can be a more efficient alternative for time-dependent problems since one only needs to solve several decoupled systems of parabolic or elliptic equations at each timestep. Standard Krylov subspace methods like the conjugate gradient method or GMRES with efficient preconditioners like multigrid or domain decomposition can then be used to solve the linear systems. The main drawback of projection methods is that high-order methods are hard to design and analyse due to the introduction of additional unphysical boundary conditions.

Valen-Sendstad et al. [6] studied the performance of six different solvers for incompressible flow and among them a Chorin projection method (incremental pressure correction) and a least-squares stabilized Galerkin scheme. From their study they conclude that the incremental pressure scheme was the most efficient and accurate method. However, this depends of course on the problem at hand. They looked at low Reynolds number cases, whereas our interest lies in high Reynolds flow.

In this paper we intend to highlight some aspects related to the quality of computed solutions and computational efficiency of three isogeometric incompressible Navier-Stokes solvers applied to a two-dimensional problem. The first solver is based on a Chorin projection method (incremental pressure correction) along with the Spalart–Allmaras turbulence model [7], the second is based on a coupled formulation of the Navier-Stokes equations combined with the Spalart-Allmaras turbulence model and the third is a variational multiscale approach [3]. Common to all methods is that the equations are discretized using linear and quadratic spline elements. As a test case we have chosen flow past a fixed two-dimensional NACA0012 airfoil, which is considered to be a relevant airfoil for wind turbine application.

The paper is organized as follows: Section 2 starts with a brief description of the family of NACA airfoils followed by the relevant governing flow equations. Then we describe the two different types of turbulence modelling approaches that we have used as well as the implementation of the Chorin and coupled Navier-Stokes solvers. Our quantities of interests are lift, drag and pressure coefficients, so their expressions are also presented. Section 3 describes the simulation setup and other simulation parameters used in the study. Finally, in Section 4 the results from the three different solvers for linear and quadratic spline elements are compared and their computational efficiencies are evaluated. The paper ends with the main conclusion of the study in Section 5.

2. Theory

2.1. Symmetric 4-digit NACA airfoils

The 4-digit NACA airfoils denote a series of airfoil shapes developed by the National Advisory Committee for Aeronautics (NACA). All NACA airfoils are identified by four digits and are usually written in the form NACA XXXX where the first digit is the maximum camber as a percentage of the chord, the second digit is the distance of maximum camber from the leading edge in percent of the chord and the last two digits are the maximal thickness as a percentage of the chord. See Figure 1 for a description of the different design parameters of the NACA airfoil. Symmetric NACA airfoils have no camber and are only
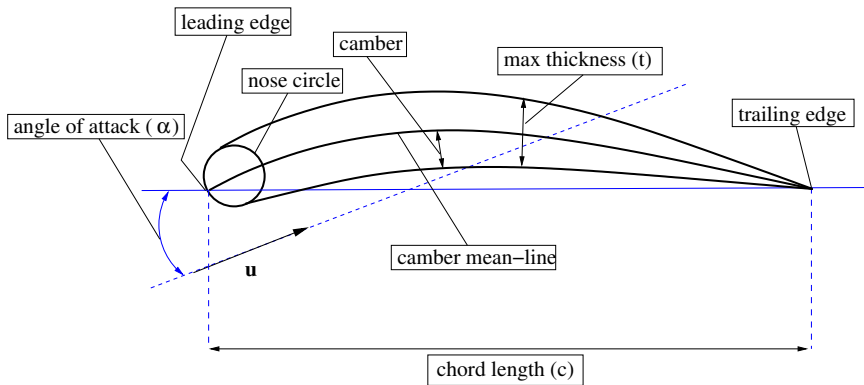

Figure 1: Design parameters for NACA XXXX airfoil.

characterized by the two last digits, i.e. the ratio between the maximal thickness t and the chord length c, see Figure 2. The shapes of these airfoils (NACA 00XX) are given by the analytical formula

$$y_t = 5tc \left[0.2969 \sqrt{\frac{x}{c}} - 0.1260 \left(\frac{x}{c}\right) - 0.3516 \left(\frac{x}{c}\right)^2 + 0.2843 \left(\frac{x}{c}\right)^3 - 0.1015 \left(\frac{x}{c}\right)^4 \right]$$

(1)

where y_t is the distance from the centerline, t is the maximal thickness from centerline, c is the chord length and x is the position along the chord from 0 to c. The Equation (1) does not give a closed curve for the wing profile since y is not exactly 0 for $x = c$. To get a closed curve the last coefficient is modified to
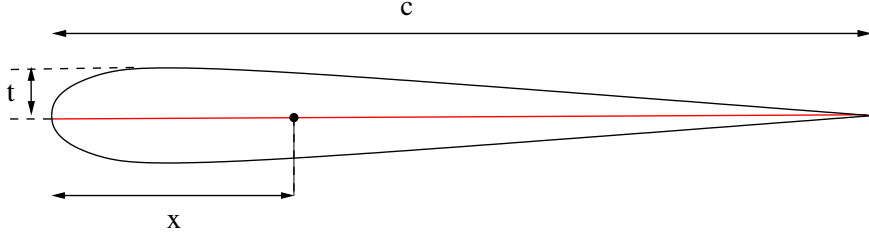
3

Figure 2: Symmetric NACA 00XX airfoil.

get

$$y_t = 5tc \left[0.2969\sqrt{\frac{x}{c}} - 0.1260\left(\frac{x}{c}\right) - 0.3516\left(\frac{x}{c}\right)^2 + 0.2843\left(\frac{x}{c}\right)^3 - 0.1036\left(\frac{x}{c}\right)^4 \right]$$

(2)

This formula has been used to approximate the NACA0012 wing profile in the numerical investigation presented in this paper.

2.2. Governing equations

Subsonic, viscous flows is mathematically described by the incompressible Navier-Stokes equations given by

$$\rho\frac{\partial \boldsymbol{u}}{\partial t} + \rho\left(\boldsymbol{u}\cdot\nabla\right)\boldsymbol{u} - \nabla\cdot\boldsymbol{\sigma}\left(\boldsymbol{u}, p\right) = \rho\boldsymbol{f} \quad \text{in } \Omega$$

$$\nabla\cdot\boldsymbol{u} = 0 \quad \text{in } \Omega.$$

(3)

Here, $\Omega \in \mathbb{R}^d$, $d = 2, 3$, is a suitable, sufficiently regular and open domain, ρ the constant fluid density, p the pressure, $\boldsymbol{u}$ the fluid velocity vector and $\boldsymbol{f}$ a volumetric body force. The Cauchy stress tensor can be written as

$$\boldsymbol{\sigma}(\boldsymbol{u}, p) = -p\boldsymbol{I} + 2\mu\boldsymbol{\epsilon}(\boldsymbol{u}),$$

where $\boldsymbol{I}$ is the identity tensor, μ the dynamic viscosity and the strain rate $\boldsymbol{\epsilon}$ is defined as

$$\boldsymbol{\epsilon}(\boldsymbol{u}) = \frac{1}{2}\left(\nabla\boldsymbol{u} + (\nabla\boldsymbol{u})^T\right).$$

We also define $\partial\Omega = \Gamma = \Gamma_D \cup \Gamma_N \cup \Gamma_M$ where Γ_D are the boundaries with Dirichlet conditions, Γ_N the boundaries with Neumann conditions Γ_M the boundaries with mixed conditions. Mixed boundary conditions are used in situations where the normal velocity components is given, usually zero, together with the tangential stresses can model symmetry planes and slip or friction conditions.

The variational formulation is expressed as: Find $(\boldsymbol{u}, p) \in \boldsymbol{U} \times Q$ such that

$$\left(\rho\frac{\partial \boldsymbol{u}}{\partial t}, \boldsymbol{v}\right) + c(\boldsymbol{u}; \boldsymbol{u}, \boldsymbol{v}) + b(p, \boldsymbol{v}) + a(\boldsymbol{u}, \boldsymbol{u}) + b(q, \boldsymbol{u}) = f(\boldsymbol{v}) \quad (\boldsymbol{v}, q) \in \boldsymbol{V} \times Q,$$

(4)

where we have defined the spaces

$$\boldsymbol{U} = \boldsymbol{H}_{\Gamma_D, \Gamma_M^\perp}(\Omega) = \left\{\boldsymbol{v} \in \boldsymbol{H}^1(\Omega) \mid \boldsymbol{v} = \boldsymbol{u_D} \text{ on } \Gamma_D \text{ and } \boldsymbol{v}\cdot\boldsymbol{n} = u_\perp \text{ on } \Gamma_M\right\}$$

$$\boldsymbol{V} = \boldsymbol{H}_{\Gamma_D, \Gamma_M^\perp; 0}(\Omega) = \left\{\boldsymbol{v} \in \boldsymbol{H}^1(\Omega) \mid \boldsymbol{v} = 0 \text{ on } \Gamma_D \text{ and } \boldsymbol{v}\cdot\boldsymbol{n} = 0 \text{ on } \Gamma_M\right\}$$

$$Q = L^2(\Omega),$$

4

where $\boldsymbol{u_D}$ and $u_\perp$ both are given functions and $\boldsymbol{n}$ is the unit outer normal on Γ, and the forms

$$a(\boldsymbol{u}, \boldsymbol{v}) = 2 \int_\Omega \mu \boldsymbol{\epsilon}(\boldsymbol{u}) : \boldsymbol{\epsilon}(\boldsymbol{v}) \, \mathrm{d}\boldsymbol{x}$$

$$b(q, \boldsymbol{v}) = - \int_\Omega (\nabla \cdot \boldsymbol{v}) q \, \mathrm{d}\boldsymbol{x}$$

$$c(\boldsymbol{w}; \boldsymbol{u}, \boldsymbol{v}) = \int_\Omega \rho(\boldsymbol{w} \cdot \nabla)\boldsymbol{u} \cdot \boldsymbol{v} \, \mathrm{d}\boldsymbol{x}$$

$$f(\boldsymbol{v}) = \int_\Omega \rho \boldsymbol{f} \cdot \boldsymbol{v} \, \mathrm{d}\boldsymbol{x} + \int_{\Gamma_N} \boldsymbol{t} \cdot \boldsymbol{v} \, \mathrm{d}\boldsymbol{s},$$

where $\boldsymbol{t} = \boldsymbol{\sigma} \cdot \boldsymbol{n}$ is the traction vector on Γ.

2.2.1. Isogeometric finite element approximation

The isogeometric finite element method approximates the solution by using a spline basis of polynomial order p and regularity C^{p-1}, whereas C^0 Lagrange polynomials of low order (typical $p = 1$ or $p = 2$) are used in traditional finite element formulations. Our approach is based on a conforming finite element approximation, i.e.

$$\boldsymbol{U}_h \subset \boldsymbol{U}, \quad \boldsymbol{V}_h \subset \boldsymbol{V}, \quad Q_h \subset Q.$$

The discrete approximation spaces $\boldsymbol{U}_h$, $\boldsymbol{V}_h$, Q_h are chosen as the isogeometric finite element spaces. This gives the semi-discrete formulation of the variational problem stated in Eq. (4): Find $(\boldsymbol{u}_h, p_h) \in \boldsymbol{U}_h \times Q_h$ such that

$$\left(\rho \frac{\partial \boldsymbol{u}_h}{\partial t}, \boldsymbol{v}_h \right) + c(\boldsymbol{u}_h; \boldsymbol{u}_h, \boldsymbol{v}_h) + a(\boldsymbol{u}_h, \boldsymbol{u}_h) + b(p, \boldsymbol{v}_h) + b(q, \boldsymbol{u}_h) = f(\boldsymbol{v}_h)$$

for all $(\boldsymbol{v}_h, q_h) \in \boldsymbol{V}_h \times Q_h$.

Herein, we have developed a block-structured B-spline isogeometric finite element approximation of the Navier-Stokes equations described above. To construct a B-spline basis for a domain Ω which is subdivided into a number of patches (a patch is equivalent to a block) Ω_e such that $\Omega = \cup_{e=1}^N \Omega_e$ we associate for each patch a knot-vector in each coordinate direction

$$\Xi_k^e = \left\{ \xi_{1,k}^e, \xi_{2,k}^e, \dots, \xi_{n_k^e + p_k^e + 1}^e \right\}$$

for $k = 1, \dots, d$. The B-spline basis for patch Ω_e on the parametric domain $\hat{\Omega} = (0,1)^d$ is written as $\hat{\boldsymbol{S}}_{\boldsymbol{\alpha}^e}^{\boldsymbol{p}^e}$ where the multi-indices $\boldsymbol{\alpha}^e = (\alpha_1^e, \dots, \alpha_d^e)$ and $\boldsymbol{p}^e = (p_1^e, \dots, p_d^e)$ denote the regularity and order for the basis in each coordinate direction, respectively. The corresponding basis for the physical domain Ω_e can be expressed using the coordinate mapping $\phi_e : \hat{\Omega} \to \Omega_e$ as

$$\boldsymbol{S}_{\boldsymbol{\alpha}^e}^{\boldsymbol{p}^e} = \left\{ v_h \mid v_h \circ \boldsymbol{\phi}_e \in \hat{\boldsymbol{S}}_{\boldsymbol{\alpha}^e}^{\boldsymbol{p}^e} \right\}.$$

If the variational formulation allows a discontinuous approximation the spline finite element basis for the domain Ω can be defined as

$$\boldsymbol{S}_h = \left\{ v_h \mid v_{h|\Omega_e} \in \boldsymbol{S}_{\boldsymbol{\alpha}^e}^{\boldsymbol{p}^e} \right\}.$$

If we assume that the knot-vectors and geometrical mapping $\boldsymbol{\phi}_e$ for all the patches are consistent on common edges and faces we can define a continuous basis

$$\boldsymbol{\mathcal{S}_h} = \left\{ v_h \in C(\Omega) \mid v_{h|\Omega_e} \in \boldsymbol{\mathcal{S}^{p^e}_{\alpha^e}} \right\}.$$

We use the same basis for the geometry as for the discretization of the velocity and the pressure.

2.3. Turbulence modelling

High Reynolds number flows involving reasonably complex geometries like airfoils are mostly turbulent and require turbulence modelling since their explicit resolution using Direct Numerical Simulation (DNS) is still computationally intractable. Thus one is left with either of the two choices Reynolds Averaged Navier Stokes (RANS) or Large Eddy Simulation (LES) based models. In the former all the scales are modelled while in the latter only the small isotropic scales are modelled while the larger energy-containing scales are resolved. In the present study we use the Spalart-Allmaras model and variational multiscale model which can be seen to lie in the category of RANS and LES classes. A brief discussion of the models is presented in the following subsections.

2.3.1. Spalart-Allmaras model

In RANS models the flow is divided into a time-averaged and fluctuating part known as *Reynolds decomposition*

$$\boldsymbol{u} = \bar{\boldsymbol{u}} + \boldsymbol{u}',$$
$$p = \bar{p} + p',$$

where $\bar{\boldsymbol{u}}$, $\bar{p}$ are the time-averaged components while the $\boldsymbol{u}'$, p' are the fluctuations in time. The Navier–Stokes equations are then time-averaged to give an equation for the time-averaged quantities. Assuming that the time average of the fluctuation part is zero, the Reynolds averaged Navier–Stokes equations can be written as

$$\rho \left(\frac{\partial \bar{\boldsymbol{u}}}{\partial t} + (\bar{\boldsymbol{u}} \cdot \nabla)\bar{\boldsymbol{u}} \right) - \nabla \cdot (\boldsymbol{\sigma}(\bar{\boldsymbol{u}}, \bar{p}) + \rho \langle \boldsymbol{u}' \otimes \boldsymbol{u}' \rangle) = \rho \bar{\boldsymbol{f}},$$

$$\nabla \cdot \bar{\boldsymbol{u}} = 0,$$

where $\langle \cdot \rangle$ is the averaging operator and $(\langle \boldsymbol{u}' \otimes \boldsymbol{u}' \rangle)_{ij} = \langle u_i' u_j' \rangle$. The equations have a form similar to the original Navier–Stokes equations except for the last term on the left hand side of the momentum equation which results from the time averaging and acts similar to the viscous stress term and is therefore called the *Reynolds stress* term. The Reynolds stress tensor is symmetric and introduces new unknowns, 6 in 3D and 3 in 2D, and therefore additional equations are required to close the system. In the present study we employ the Spalart-Allmaras model [7]. This model solves a scalar transport equation for the modified kinematic viscosity parameter $\tilde{\nu}$. The formulation of the model is the transport equation

$$\frac{\partial \tilde{\nu}}{\partial t} + \boldsymbol{u} \cdot \nabla \tilde{\nu} = c_{b1} \tilde{S} \tilde{\nu} + \frac{1}{\sigma} \left(\nabla \cdot (\nu + \tilde{\nu}) \nabla \tilde{\nu} + c_{b2} |\nabla \tilde{\nu}|^2 \right) - c_{w1} f_w \left(\frac{\tilde{\nu}}{d} \right)^2.$$

Here $\nu = \mu/\rho$ denotes the laminar kinematic viscosity, $\boldsymbol{u}$ the fluid velocity and d the distance from a given point to the closest solid wall. From the modified viscosity the eddy viscosity can be computed as

$$\nu_t = \tilde{\nu} f_{v1}, \quad f_{v1} = \frac{\tilde{\nu}^3}{\tilde{\nu}^3 + \nu^3 c_{v1}^3}.$$

Modifications of the original model for the modified vorticity were published in [8]. The modified vorticity $\tilde{S}$ is now given by

$$\overline{S} = \frac{\tilde{\nu}}{\kappa^2 \cdot d^2} f_{v2}, \quad f_{v2} = 1 - \frac{\tilde{\nu}}{\nu + \tilde{\nu} f_{v1}}$$

where S represents the magnitude of the vorticity and d the distance to the closest wall, and

$$\tilde{S} = \begin{cases} S + \overline{S} & : \overline{S} \geq -c_{v2} S \\ S + \frac{S(c_{v2}^2 S + c_{v3} \overline{S})}{(c_{v3} - 2c_{v2})S - \overline{S}} & : \overline{S} < -c_{v2} S \end{cases}$$

with $c_{v2} = 0.7$ and $c_{v3} = 0.9$. The new modified vorticity $\tilde{S}$ does not have the possibility of becoming negative and thus avoids a possible problem of disrupting other Spalart–Allmaras functions. Furthermore we have for the destruction term

$$f_w = g \left[\frac{1 + c_{w3}^6}{g^6 + c_{w3}^3} \right]^{1/6}$$
$$g = r + c_{w2}(r^6 - r)$$
$$r = \frac{\tilde{\nu}}{\tilde{S}\kappa^2 d^2}.$$

In the original work [7] the following values were given for the constants appearing in the model

$$c_{b1} = 0.1355, \quad c_{b_2} = 0.622, \quad c_{w_2} = 0.3, \quad c_{w_3} = 2,$$
$$\sigma = 2/3, \quad c_{v1} = 7.1, \quad \kappa = 0.41.$$

To relax the need for high resolution in the mesh close to the wall the law-of-the-wall parametrization given in [8] is introduced. Here the turbulent viscosity close to the wall is approximated by an analytical expression derived for idealized flow conditions. The use of the law-of-the-wall parametrization allows for a much coarser resolution close to the wall distance $y^+ \sim 10 - 30$. Here, y^+ is the non-dimensional wall distance defined in terms of the friction or shear stress velocity u_τ as

$$y^+ = \frac{u_*}{\nu} \quad \text{with} \quad u_* = \sqrt{\frac{\tau_w}{\rho}}$$

where the wall shear stress τ_w is given by

$$\tau_w = \mu \left[\frac{\partial \boldsymbol{u}}{\partial \boldsymbol{n}} \right]_{y=0} = \mu \left[\nabla \boldsymbol{u} \cdot \boldsymbol{n} \right]_{y=0}.$$

The starting point for the derivation is the following simple solution of the SA model

$$\tilde{\nu} = \kappa u_\tau y, \qquad \tilde{S} = \frac{u_\tau}{\kappa y}, \tag{5}$$

where y is the distance from the wall. The shear stress velocity can be written as $u_\tau = u_{\text{tan}}/u^+$, where u_{tan} is the tangential velocity and u^+ the dimensionless velocity. By using the common assumptions for the derivation of wall laws, i.e. incompressible flow, zero pressure gradient, constant velocity in the outer region, negligible advection in the boundary layer, the following simplified expression for the wall law is derived

$$u^+(y^+) = \bar{B} + c_1 \log\left((y^+ + a_1)^2 + b_1^2\right)$$
$$- c_2 \log\left((y^+ + a_2)^2 + b_2^2\right) - c_3 \text{atan2}[y^+ + a_1, b_1] - c_4 \text{atan2}[y^+ + a_2, b_2]. \tag{6}$$

The atan2 function can be defined from the standard arctan function as

$$\text{atan2}(y, x) = \begin{cases} \arctan\left(\frac{y}{x}\right), & x > 0, \\ \arctan\left(\frac{y}{x}\right), & y \geq 0, \ x < 0, \\ \arctan\left(\frac{y}{x}\right), & y < 0, \ x < 0, \\ \frac{\pi}{2}, & y > 0, \ x = 0, \\ -\frac{\pi}{2}, & y < 0, \ x = 0, \\ \text{undefined}, & y = 0, \ x = 0. \end{cases}$$

Since the mean velocity u^+ is a function of the normalized wall normal distance y^+ the wall law can be explicitly evaluated and there is no need for non-linear Newton iterations. The value of the constants in Equation (6) are given by $\bar{B} = 5.0333908790505579$ and

$$a_1 = 8.148221580024245, \qquad b_1 = 7.4600876082527945,$$
$$a_2 = -6.9287093849022945, \quad b_2 = 7.468145790401841,$$
$$c_1 = 2.5496773539754747, \qquad c_2 = 1.3301651588535228,$$
$$c_3 = 3.599459109332379, \qquad c_4 = 3.6397531868684494.$$

When using the wall law a no-slip condition is used for the fluid velocity and the modified vorticity is set to zero on the walls. A Dirichlet condition based on the wall law is imposed on the near-wall nodes. On the inflow boundaries $\tilde{\nu}_{\text{in}} = 5\nu$ is used, whilst a homogeneous Neumann boundary condition is applied on the outflow boundaries and symmetry planes,

$$\frac{\partial \tilde{\nu}}{\partial \boldsymbol{n}} = \nabla \tilde{\nu} \cdot \boldsymbol{n} = 0.$$

The turbulent viscosity field computed is then used to model the Reynolds stresses [7] through the constitutive relation

$$-\langle u_i' u_j' \rangle = 2\nu_t \epsilon_{ij}.$$

and thus to close the problem.

2.3.2. Variational multiscale

The variational multiscale formulation is similar to a LES model for fluid flow but without the concept of an eddy viscosity. The starting point for the derivation of the variational multiscale formulation of the incompressible Navier–Stokes equations is the variational formulation, Equation (4). To simplify the notation we follow [3] and write $\boldsymbol{U} = (\boldsymbol{u}, p)$ and $\boldsymbol{V} = (\boldsymbol{v}, q)$ for the solutions and test functions, respectively. The corresponding functional spaces are given by

$$\mathcal{U} = \mathsf{U} \times \mathsf{Q},$$
$$\mathcal{V} = \mathsf{V} \times \mathsf{Q}.$$

The variational formulation of the incompressible Navier–Stokes problem (3) can now be written as

$$B(\boldsymbol{U}, \boldsymbol{V}) = B_L(\boldsymbol{U}, \boldsymbol{V}) + B_{NL}(\boldsymbol{U}; \boldsymbol{U}, \boldsymbol{V}) = F(\boldsymbol{V}), \qquad (7)$$

where the operator B is split into a linear and a non-linear part as

$$B_L(\boldsymbol{U}, \boldsymbol{V}) = \left(\rho \frac{\partial \boldsymbol{u}}{\partial t}, \boldsymbol{v} \right) + b(p, \boldsymbol{v}) + a(\boldsymbol{u}, \boldsymbol{v}) - b(q, \boldsymbol{u}),$$
$$B_{NL}(\boldsymbol{W}; \boldsymbol{U}, \boldsymbol{V}) = c(\boldsymbol{w}; \boldsymbol{u}, \boldsymbol{v}), \qquad (8)$$

and the linear functional is given as

$$F(\boldsymbol{V}) = f(\boldsymbol{v}).$$

Then a decomposition of the solution space $\mathcal{U}$ into a «coarse scale» $\bar{\mathcal{U}}$ and «fine scale» $\mathcal{U}'$ is defined as

$$\mathcal{U} = \bar{\mathcal{U}} \oplus \mathcal{U}'. \qquad (9)$$

It is assumed that $\bar{\mathcal{U}}$ is a finite dimensional space which in practical applications will be a numerical approximation space, for instance a finite element space. A unique decomposition (9) is defined by a projection operator $\mathbb{P} : \mathcal{U} \to \bar{\mathcal{U}}$ such that

$$\bar{\boldsymbol{U}} = \mathbb{P}\boldsymbol{U},$$
$$\boldsymbol{U}' = \boldsymbol{U} - \bar{\boldsymbol{U}} = (\mathbb{I} - \mathbb{P})\boldsymbol{U},$$

where $\mathbb{I}$ is the identity operator. The projection operator $\mathbb{P}$ can for example be the L^2- or H^1-projection onto the coarse space $\bar{\mathcal{U}}$. A similar decomposition is also introduced for the space of test functions $\mathcal{V}$ as

$$\bar{\boldsymbol{V}} = \mathbb{P}\boldsymbol{V},$$
$$\boldsymbol{V}' = (\mathbb{I} - \mathbb{P})\boldsymbol{V}.$$

Writing the solution and test functions as $\bar{\boldsymbol{U}} + \boldsymbol{U}'$ and $\bar{\boldsymbol{V}} + \boldsymbol{V}'$, respectively, the variational problems (7) reads

$$B(\bar{\boldsymbol{U}} + \boldsymbol{U}', \bar{\boldsymbol{V}} + \boldsymbol{V}') = F(\bar{\boldsymbol{V}} + \boldsymbol{V}').$$

If both $\bar{\boldsymbol{V}}$ and $\boldsymbol{V}'$ are valid test functions for the original variational formulation (7), i.e. if $\bar{\mathcal{V}} \subset \mathcal{V}$ and $\mathcal{V}' \subset \mathcal{V}$, then one can first choose $\boldsymbol{V}' = 0$ and then $\bar{\boldsymbol{V}} = 0$ to get the coarse and fine scale equations

$$B(\bar{\boldsymbol{U}} + \boldsymbol{U}', \bar{\boldsymbol{V}}) = F(\bar{\boldsymbol{V}}),$$
$$B(\bar{\boldsymbol{U}} + \boldsymbol{U}', \boldsymbol{V}') = F(\boldsymbol{V}').$$

The fine scale equation can be rephrased in the form

$$DB_{\bar{U}}(\mathbf{U}', \mathbf{V}') + B_{NL}(\mathbf{U}'; \mathbf{U}', \mathbf{V}') = \langle \mathbf{R}(\bar{U}), \mathbf{V}' \rangle_{\mathcal{V}'^*, \mathcal{V}'}$$

where $DB_{\bar{U}}$ is the linearization of B about $\bar{U}$ in the direction of $\mathbf{U}'$

$$
\begin{aligned}
DB_{\bar{U}}(\mathbf{U}', \mathbf{V}') &= \frac{d}{d\epsilon} B(\bar{U} + \epsilon \mathbf{U}', \mathbf{V}') \big|_{\epsilon=0} \\
&= B_L(\mathbf{U}', \mathbf{V}') + B_{NL}(\bar{U}; \mathbf{U}', \mathbf{V}') + B_{NL}(\mathbf{U}'; \bar{U}, \mathbf{V}')
\end{aligned}
$$

and $\mathbf{R}(\bar{U})$ is the coarse scale residual lifted to the fine scale by the duality pairing

$$\langle \mathbf{R}(\bar{U}), \mathbf{V}' \rangle_{\mathcal{V}'^*, \mathcal{V}'} = F(\mathbf{V}') - B_L(\bar{U}, \mathbf{V}') - B_{NL}(\bar{U}; \bar{U}, \mathbf{V}').$$

The fine scale solution can formally be written as a functional of the form

$$\mathbf{U}' = \mathbf{F}'(\bar{U}, \mathbf{R}(\bar{U})),$$

and then the equation for the finite dimensional coarse scale solution $\bar{U}$ can be written as

$$B(\bar{U} + \mathbf{F}'(\bar{U}, \mathbf{R}(\bar{U})), \bar{V}) = L(\bar{V}).$$

So far no approximations have been introduced, and thus the exact solution of the Navier-Stokes problem (7) is given by $\mathbf{U} = \bar{U} + \mathbf{U}'$. However, in practice we are not able to obtain an analytical expression for the fine scale solution and some kind of approximation must be introduced.

The turbulence modelling concept introduced in [3] is based on approximating the functional $\mathbf{F}'$ and thus find an approximate fine scale solution $\mathbf{U}'$. The fine scale solution is then substituted into the coarse scale equation which then can be solved for $\bar{U}$. Hence the variational multiscale approach to turbulence modelling can be written as

$$\tilde{\mathbf{U}}' = \tilde{\mathbf{F}}'(\tilde{\bar{U}}, \mathbf{R}(\tilde{\bar{U}})),$$
$$B(\tilde{\bar{U}} + \tilde{\mathbf{F}}'(\tilde{\bar{U}}, \mathbf{R}(\tilde{\bar{U}})), \bar{V}) = L(\bar{V}),$$

where $\tilde{\mathbf{F}}'$ is an approximation to $\mathbf{F}'$, and $\tilde{\bar{U}}$ and $\tilde{\mathbf{U}}'$ are approximations to $\bar{U}$ and $\mathbf{U}'$, respectively. In the turbulence model introduced in [3] the approximation of the fine scale $\tilde{\mathbf{U}}'$ is based on

1. The expression of the fine scale solution $\mathbf{U}'$ as a perturbation series of the form

$$\mathbf{U}' = \epsilon \mathbf{U}_1' + \epsilon^2 \mathbf{U}_2' + \cdots = \sum_{k=1}^{\infty} \epsilon^k \mathbf{U}_k'$$

   with $\epsilon = \|\mathbf{R}(\bar{U})\|_{\mathcal{V}'^*}$.

2. Truncation of the perturbation series after the first term

$$\mathbf{U}' \approx \epsilon \mathbf{U}_1'.$$

3. An approximation of the fine scale Green's operator for the linearized Navier–Stokes equations is defined as $\tilde{\mathbf{G}}'_{\bar{U}} \approx \mathbf{G}'_{\bar{U}}$, and it is used to find an approximate solution for $\mathbf{U}_1$.

4. Traditional SUPG and residual based stabilization methods have been shown to represent local approximations of the fine scale Green's operator, see [9, 10, 11, 12]. Hence, a simple approximation of the fine scale field can be written as

$$\tilde{\boldsymbol{U}}' \approx -\boldsymbol{\tau}\boldsymbol{R}(\tilde{\tilde{\boldsymbol{U}}}) \tag{10}$$

where the matrix $\boldsymbol{\tau} \in \mathbb{R}^{4\times 4}$ can be computed element-wise as the mean value of the fine scale Green's operator over the element. Usually $\boldsymbol{\tau}$ is taken to be a diagonal matrix on the form

$$\boldsymbol{\tau} = \begin{pmatrix} \tau_M \boldsymbol{I}_{3\times 3} & \boldsymbol{0} \\ \boldsymbol{0} & \tau_C \end{pmatrix}.$$

For more details on the derivation of the variational multiscale formulation of turbulent incompressible flow presented above we refer to Bazilevs et al. [3]. For a detailed study of the fine scale Green's operator for the linear, steady advection-diffusion equation, see Hughes and Sangalli [12].

Substituting the fine scale approximation given by Equation (10) into the variational formulation given by Equation (7) gives the following final formulation: Find $\boldsymbol{U}_h \in \mathcal{U}_h$ such that

$$B_h^{ms}(\boldsymbol{U}_h, \boldsymbol{V}_h) = L(\boldsymbol{V}_h) \tag{11}$$

where

$$B_h^{ms}(\boldsymbol{U}_h, \boldsymbol{V}_h) = B(\boldsymbol{U}_h, \boldsymbol{V}_h) + B_h'(\boldsymbol{U}_h, \boldsymbol{V}_h) \tag{12}$$

and the additional terms are given by

$$
\begin{aligned}
B_h'(\boldsymbol{U}_h, \boldsymbol{V}_h) = {} & \left(\boldsymbol{u}_h \cdot \nabla \boldsymbol{v}_h + \frac{\nabla q_h}{\rho}, \tau_M \boldsymbol{r}_M(\boldsymbol{u}_h, p_h) \right) \\
& + (\rho \nabla \cdot \boldsymbol{v}_h, \tau_C r_c(\boldsymbol{u}_h)) \\
& + \left(\boldsymbol{u}_h \cdot (\nabla \boldsymbol{v}_h)^T, \tau_M \boldsymbol{r}_M(\boldsymbol{u}_h, p_h) \right) \\
& - \left(\frac{\nabla \boldsymbol{v}_h}{\rho}, \tau_M \boldsymbol{r}_M(\boldsymbol{u}_h, p_h) \otimes \tau_M \boldsymbol{r}_M(\boldsymbol{u}_h, p_h) \right).
\end{aligned}
\tag{13}
$$

Here $\boldsymbol{r}_M$ and r_C denote the residual of the momentum and continuity equation, that is

$$\boldsymbol{r}_M(\boldsymbol{u}_h, p_h) = \rho \frac{\partial \boldsymbol{u}_h}{\partial t} + \rho \boldsymbol{u}_h \cdot \nabla \boldsymbol{u}_h + \nabla p_h - \mu \Delta \boldsymbol{u}_h - \rho \boldsymbol{f},$$

$$r_C(\boldsymbol{u}_h) = \nabla \cdot \boldsymbol{u}_h.$$

The non-conservative formulation is used for the definition of the momentum residual in the terms corresponding to the VMS stabilization terms. It is reported in [3] that this has a favorable effect on the stability of the formulation compared with the conservative formulation. We note that he first two terms on the right-hand side of Equation (13) represent the standard SUPG, pressure and continuity stabilization terms, while the last two terms are unique for the variational multiscale formulation. The variational multiscale turbulence model defined by Equations (11)-(13) has been applied to forced homogeneous isotropic turbulence and turbulent channel flows with very good results in [3].

2.4. Coupled Navier-Stokes RANS

In this work using a coupled Navier-Stokes solver in a RANS setting is considered. Here one solves the variational problem: Find $\boldsymbol{U}_h \in \mathcal{U}_h$ such that

$$B_h(\boldsymbol{U}_h, \boldsymbol{V}_h) = L(\boldsymbol{V}_h) \tag{14}$$

where

$$B_h(\boldsymbol{U}_h, \boldsymbol{V}_h) = B(\boldsymbol{U}_h, \boldsymbol{V}_h) + B'_h(\boldsymbol{U}_h, \boldsymbol{V}_h) \tag{15}$$

and the additional terms are given by

$$\begin{aligned}
B'_h(\boldsymbol{U}_h, \boldsymbol{V}_h) = {} & \left(\boldsymbol{u}_h \cdot \nabla \boldsymbol{v}_h + \frac{\nabla q_h}{\rho}, \tau_M \boldsymbol{r}_M(\boldsymbol{u}_h, p_h) \right) \\
& + (\rho \nabla \cdot \boldsymbol{v}_h, \tau_C r_c(\boldsymbol{u}_h))
\end{aligned} \tag{16}$$

This is Equation (13) without the extra multiscale terms, i.e., the Reynolds-averaged Navier-Stokes equations with SUPG, continuity and pressure stabilization terms, where the Spalart–Allmaras model is used for the Reynolds stress terms.

2.5. The Chorin scheme

The projection methods were introduced in the late 1960s by Chorin [13] and Temam [14]. Here one only needs to solve decoupled problems of elliptic equations at each timestep instead of the full coupling of the velocity and pressure [15]. Thus standard Krylov subspace methods like the Conjugate Gradient (CG) method and Generalized Minimal RESidual method (GMRES) can be used to solve the linear systems, and one can readily construct efficient preconditioners. Drawbacks of the projection methods include an inherent splitting error and erroneous numerical boundary conditions for the pressure, causing a reduced convergence order for the pressure and erroneous boundary layers in the velocity.

In order to avoid the inconsistent pressure boundary condition present in many splitting schemes we choose a rotational formulation for the incremental pressure correction scheme as proposed in [16]. This gives us the following formulation

1. Velocity prediction step

$$\begin{aligned}
\frac{\rho}{2\Delta t} \left(3\bar{\boldsymbol{u}}^{n+1} - 4\boldsymbol{u}^n + \boldsymbol{u}^{n-1} \right) + \rho \left(2\boldsymbol{u}^n - \boldsymbol{u}^{n-1} \right) \cdot \nabla \bar{\boldsymbol{u}}^{n+1} & \\
- \nabla \cdot \sigma \left(\bar{\boldsymbol{u}}^{n+1}, p^n \right) & = \rho \boldsymbol{f}^{n+1} \\
\bar{\boldsymbol{u}}^{n+1} & = 0 \text{ on } \Gamma.
\end{aligned}$$

2. Pressure correction step

$$\begin{aligned}
\frac{\rho}{2\Delta t} \left(3\boldsymbol{u}^{n+1} - \bar{\boldsymbol{u}}^{n+1} \right) + \nabla \phi^{n+1} & = 0 \\
\nabla \cdot \boldsymbol{u}^{n+1} & = 0 \\
\boldsymbol{u}^{n+1} \cdot \boldsymbol{n} & = 0 \text{ on } \Gamma,
\end{aligned}$$

with

$$\phi^{n+1} = p^{n+1} - p^n - \mu \left(\nabla \cdot \bar{\boldsymbol{u}}^{n+1} \right).$$

The term "rotational" comes from the fact that if we add the two substeps together and use the vector identity

$$-\Delta \boldsymbol{u} + \nabla \left(\nabla \cdot \boldsymbol{u} \right) = \nabla \times \nabla \times \boldsymbol{u}$$

we get

$$\frac{\rho}{3\Delta t} \left(3\boldsymbol{u}^{n+1} - 4\boldsymbol{u}^n + \boldsymbol{u}^{n-1} \right) + \rho \left(2\boldsymbol{u}^n - \boldsymbol{u}^{n-1} \right) \cdot \nabla \bar{\boldsymbol{u}}^{n+1}$$
$$+ \nabla p^{n+1} + \mu \nabla \times \nabla \times \bar{\boldsymbol{u}}^{n+1} = \rho \boldsymbol{f}^{n+1},$$
$$\nabla \cdot \boldsymbol{u}^{n+1} = 0,$$
$$\boldsymbol{u}^{n+1} \cdot \boldsymbol{n} = 0 \text{ on } \Gamma.$$

Furthermore, from the pressure correction step we see that

$$\nabla \times \nabla \times \bar{\boldsymbol{u}}^{n+1} = \nabla \times \nabla \boldsymbol{u}^{n+1},$$

and $\bar{\boldsymbol{u}}^{n+1}$ can also be replaced by $\boldsymbol{u}^{n+1}$ without affecting the accuracy of the scheme. We can also deduce the following Neumann condition for the pressure

$$\frac{\partial p}{\partial \boldsymbol{n}} = \left(\rho \boldsymbol{f}^{n+1} - \rho \left(2\boldsymbol{u}^n - \boldsymbol{u}^{n-1} \right) \cdot \nabla \boldsymbol{u}^{n+1} + \mu \nabla \times \nabla \times \boldsymbol{u}^{n+1} \right) \cdot \boldsymbol{n} \text{ on } \Gamma,$$

which is a consistent boundary condition. The resulting splitting error is only due to the slip condition imposed on the velocity. In this work this is combined with the Spalart–Allmaras turbulence model in order to perform RANS simulations.

2.6. Aerodynamic coefficients

The quantities of interest in numerical simulations of flow past an airfoil are the aerodynamic coefficients for a given angle of attack α and a given Reynolds number Re. The Reynolds number is defined as

$$Re = \frac{u_\infty c}{\nu},$$

where u_∞ is the the constant inflow velocity, c is the chord length and $\nu = \mu/\rho$ is the kinematic viscosity. The three coefficients are the drag coefficient C_D, the lift coefficient C_L and the pressure coefficient C_P defined as

$$C_D = \frac{F_x}{\frac{1}{2}\rho u_\infty^2 cl}, \quad C_L = \frac{F_y}{\frac{1}{2}\rho u_\infty^2 cl}, \quad C_P = \frac{p - p_\infty}{\frac{1}{2}\rho u_\infty^2}.$$

The quantities F_x and F_y are the horizontal and vertical force components acting on the airfoil respectively, ρ is the density of the fluid, l is the length in the spanwise direction and p_∞ is the ambient pressure. The force components are computed as

$$F = [F_x, F_y]^T = \int_{\Gamma_w} \boldsymbol{\sigma} \cdot \boldsymbol{n} \, \mathrm{d}\boldsymbol{s},$$

where Γ_w is the airfoil surface.

3. Simulation setup

Reliable results from the simulations of flow past an airfoil at high Reynolds number require a high quality mesh, properly chosen initial and boundary condition, time step for the simulation as well as the duration for which the simulations have to be run to achieve statistical convergence. Since one of the objectives of this study is the inter-comparison of the computational efficiencies of different methods, these parameters have been so chosen that they are valid and identical across all simulations. This simply means that we might be using smaller time steps or higher resolution or longer integration time than required in some cases. Optimization of these parameters for each solver is not considered here. However, important differences between the solvers will be pointed out.

3.1. Domain size and mesh resolution

The mesh is denoted S1 and have two variants: the first one based on linear spline elements and the other on quadratic spline elements. In all other aspects the meshes are similar. The meshes used throughout all the simulations have the same number of elements in order to better compare how each solver fare for the same number of degrees-of-freedom. Along the airfoil surface the meshes have 127 points with a grading factor of 0.96 towards each end. The mesh is designed iteratively for an average $y^+ = 30$ for all Spalart-Allmaras runs with wall function. This ensures that the first node close to the wall is well outside the viscous as well as the buffer layer but within the log layer. For the VMS simulations the same mesh was slightly refined so that after the simulation an average $y^+ = 10$ was obtained. Details about the mesh can be found in Table 1. The mesh is shown in Figure 3 for $\alpha = 8°$ and $p = 2$. Each mesh consists of 128 patches, of which the layout is shown in Figure 4.

Table 1: NACA0012: Detailed information about simulation mesh S1.

Mesh	S1	S1
p	1	2
n_{el}	34104	34104
n_{dof}	103539	117069

3.2. Initial and boundary conditions

For all simulations a fluid density of $\rho = 1.205$ kg/m^3 and a dynamic viscosity $\mu = 1.8208 \times 10^{-5}$ kg/(m s) are used. The inflow velocity is ramped up to a value of $u_\infty = 45.331$ m/s. The ramping function is given by:

$$u_\infty(t) = \begin{cases} u_\infty \frac{1-\cos(\pi t)}{2} & t < 1.0 \\ u_\infty & \text{otherwise.} \end{cases}$$

All the simulations involving the Chorin and coupled solver with the Spalart-Allmaras turbulence model make use of a no-slip condition on the airfoil surface. For simulations with the VMS solver a weak Dirichlet condition is applied on this boundary. A slip boundary condition is imposed on the top and bottom boundaries. At the outflow a homogeneous Neumann condition for velocity is imposed. The computational domain is shown in Figure 5.

14

3.3. Time step determination

Determining a sufficiently small time step is crucial for the convergence of the simulations. In order to determine such a time step, simulations with all three solvers for an angles of attack $\alpha = 16°, 20°$ until a non-dimensional time $t = 150$ were conducted. These two angles of attack are considered to be the most challenging of our chosen angles of attack because stall is expected at or around these cases. It was found that the biggest time step was $\Delta t = 0.00025$ that could be used with all three solvers without any issue with convergence. We can therefore conclude that the Courant-Friedrichs-Lewy (CFL) condition, which is necessary for stability, is satisfied for all the simulations. It was evident that the time step restriction is stricter for the VMS simulations than for those based on the RANS model. However, for comparison reasons, all the simulations are run with the same time step.

3.4. Simulation length

The values of drag and lift coefficients change with time and at some point attain a somewhat constant value. We treat this as a warm-up period and do

(a) NACA0012: Mesh S1   (b) NACA0012: Closeup view of mesh S1
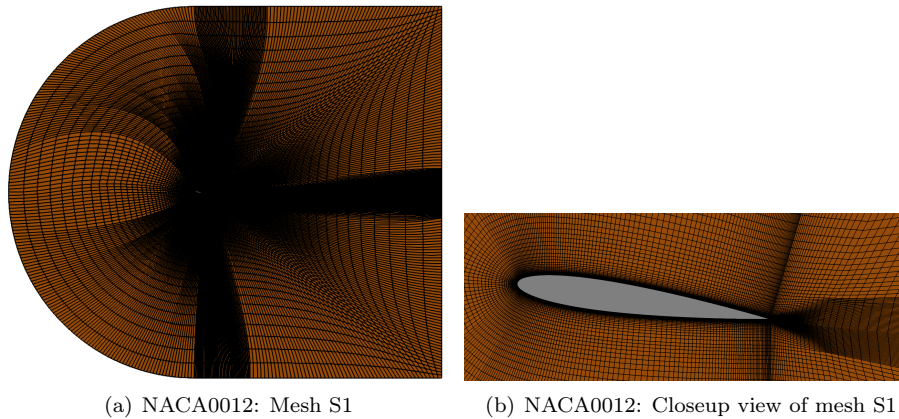
Figure 3: NACA0012: Mesh S1 for $\alpha = 8°$ and $p = 2$
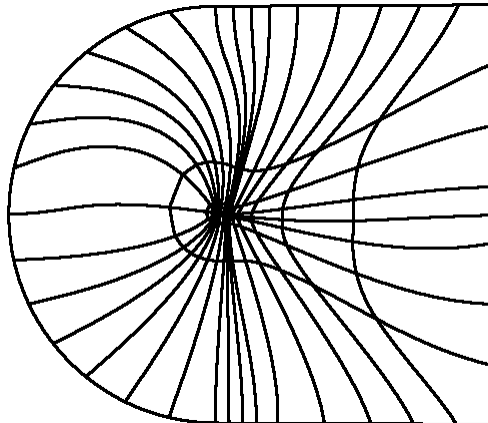
Figure 4: NACA0012: Patch layout for all meshes, here shown for $\alpha = 8°$.
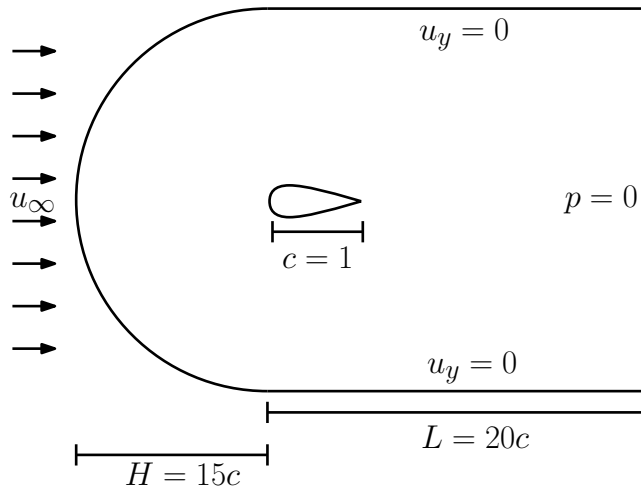
Figure 5: NACA0012: Computational domain for fixed NACA0012 airfoil.

not use the period in computing the time-averaged quantities. For the VMS simulations the warm-up period is significantly larger than the RANS simulations. In a RANS approach (in this case Spalart–Allmaras) the equations are time-averaged and then solved, while in LES (VMS in this case) the equations are solved and then the desired quantities are time averaged. The time-averaging requires that most of the flow realizations have been taken into account in the averaging procedure. It is because of this reason that one needs to use much larger time interval over which averaging is conducted. In order to get some idea about the total simulation length a case with an angle of attack of $\alpha = 16°$ was run and evolution of drag and lift coefficients were monitored. These quantities are plotted in Figure 6. It is clear from the figure that the SA results have already converged for $t < 60$ s. However, for the VMS simulations the averaging procedure can start only after $t > 100$ s. To be consistent all the simulations have been run till $t = 150$ s, i.e. 600000 timesteps, and the reported quantities are based on the averaging between $t = 125 - 150$ s.

3.5. Definition of test cases

Four angles of attack ($\alpha = 0°, 8°, 16°, 20°$) have been chosen for the investigation. Six simulations have been conducted using VMS, Chorin with Spalart-Allmaras and coupled solver with Spalart-Allmaras for linear and quadratic spline elements. All inputs, including domain size, mesh resolution, boundary conditions, initial condition and simulation time step are identical for all the simulations as explained above. This amounts to a total of 24 simulations under investigation. In addition, similar simulations are conducted with all three solvers for linear and quadratic spline elements for angles of attack of $\alpha = 4°, 10°, 12°, 14°, 18°$. These 30 cases are only used for lift and drag analysis and to populate Figure 7.

4. Results and Discussion

In this section we present a comparison of the results produced by different methods and turbulence models. We have also taken some data from the simula-
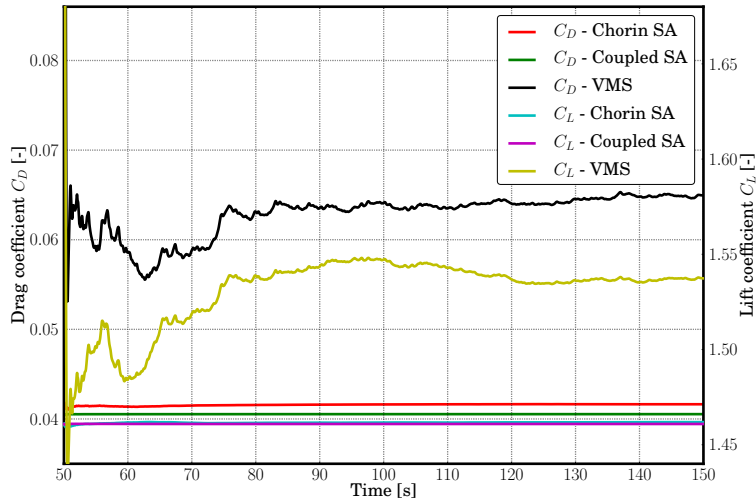
16

Figure 6: NACA0012: Cumulative mean of C_D and C_L calculated from $t = 50$ s for grid S1, $p = 2$, $\alpha = 16°$, $\Delta t = 0.00025$ using all three solvers.

tions conducted by Eleni, see [17]. Those simulations were conducted using the commercial finite volume code FLUENT using $k - \omega$ and Spalart-Allmaras turbulence models. The experimental results used for validation purpose are due to Abbott, see [18]. We also compare our simulation results to Xfoil runs. Xfoil is a freely distributed software package which can be used for estimating lift, drag and pressure distributions based on 2D airfoil profiles [19]. The results presented here are based on Xfoil runs in viscous mode at the correct Reynolds number with free transition. For the sake of convenience, in the rest of the paper, we use VMSp1, VMSp2, ChorinSAp1, ChorinSAp2, CoupledSAp1 and CoupledSAp2 to address different simulations. The convention is self-explanatory.

4.1. Lift, drag and pressure coefficients

For flow around a NACA0012 airfoil it has been observed that the lift increases linearly with the angle of attack up to an angle of approximately 17° after which there is a sudden drop in the lift coefficient and a corresponding increase in the drag coefficient. This condition is referred to as stall. A plot of experimental values of C_D and C_L along with the numerically computed values are presented in Figure 7. It is clear from the figure that it is relatively easier to predict these quantities up to an angle of 15° before which the flow is attached to the airfoil surface. Different simulations produce almost identical results. However, beyond this angle of attack stall is experienced, characterized by flow separation and different methods/models behave differently resulting in a wide spread of lift and drag coefficients. In the following subsections we explain the flow characteristics for the four different angles of attack investigated in this work in more detail.

17

Table 2: NACA0012: Lift and drag coefficients for flow past a fixed NACA0012 airfoil at $\alpha = 0°$ and $Re = 3 \times 10^6$.

	Grid	p	Δt	C_L	C_D
IFEM (ChorinSAp1)	S1	1	0.00025	−0.0006	0.0082
IFEM (ChorinSAp2)	S1	2	0.00025	0.0004	0.0119
IFEM (CoupledSAp1)	S1	1	0.00025	0.0000	0.0079
IFEM (CoupledSAp2)	S1	2	0.00025	0.0000	0.0112
IFEM (VMSp1)	S1	1	0.00025	0.0006	0.0029
IFEM (VMSp2)	S1	2	0.00025	−0.0005	−0.0188
Xfoil				0.0000	0.0051
ANSYS Fluent (SA) [17]				0.0070	0.0090
ANSYS Fluent ($k - \omega$ SST) [17]				0.0070	0.0090
Exp: Abbott et al. [18]				0.0040	0.0000

4.1.1. Results for $\alpha = 0°$

For $\alpha = 0°$ lift and drag coefficients computed by different simulations are presented in a tabular format in Table 2. As is evident from the table, all the simulations give a value of C_L and C_D close to the observation. This is quite expected. The aerodynamic design of the airfoil ensures that the body
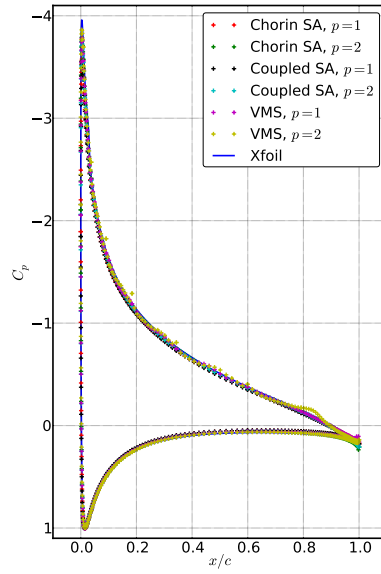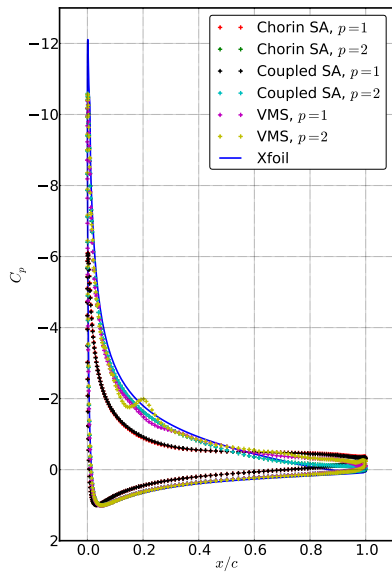

(a) C_L

(b) C_D
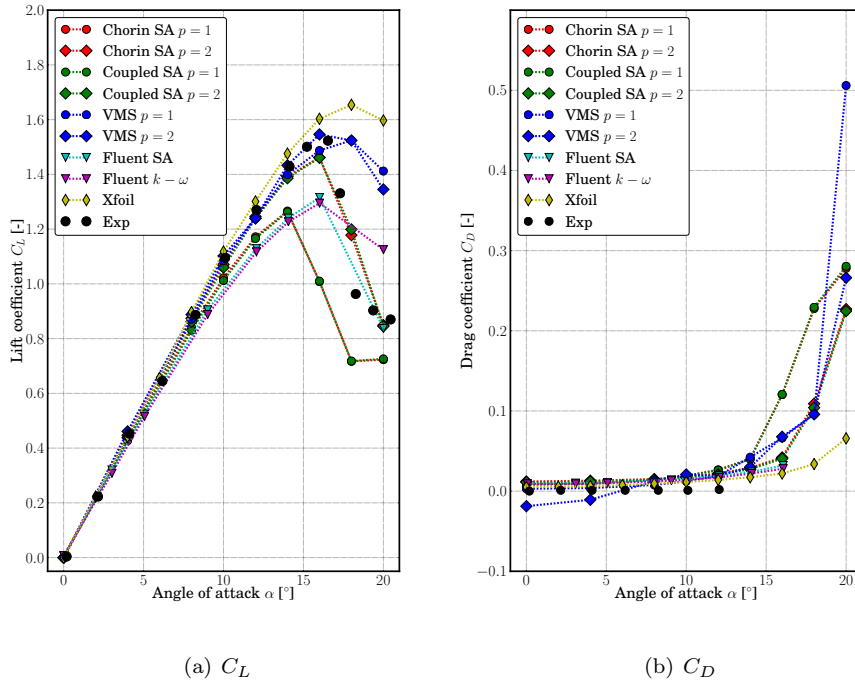
Figure 7: NACA0012: Lift and drag coefficients for different combinations of solvers and turbulence models and for different angles of attack.
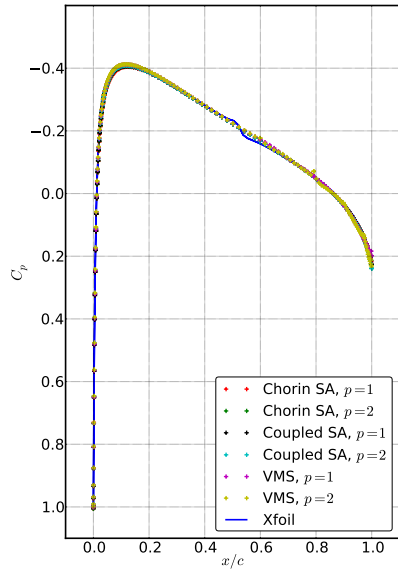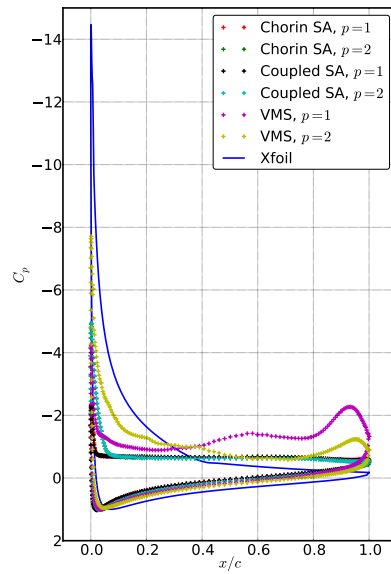
(a) $\alpha = 0°$

(b) $\alpha = 8°$

(c) $\alpha = 16°$

(d) $\alpha = 20°$

Figure 8: NACA0012: Surface pressure distributions.

19

experiences very small drag force while the perfect symmetry along the centerline ensures that the flow characteristics on the top and bottom surface of the airfoil are exactly the same. The computed pressure contours presented in Figures 9 and 10 do show a symmetric pressure distribution about the center line. The vertical component of the pressure forces integrated over the top surface is balanced by those integrated over the bottom surface resulting in zero lift. Also, as can be seen in Figures 11 and 12 the flow field is perfectly symmetric as expected. The streamlines show that the flow is strongly attached to the airfoil. The vertical component of the resultant of shear forces integrated over the top and bottom surfaces will therefore cancel each other. It should be mentioned that in reality owing to inherent unsteadiness in the flow the drag and lift coefficients can show some variations over time however, in experimental results only the time averaged quantities are reported. Such variations were also present in the numerical simulations so the reported results were averaged over time as described earlier. The pressure coefficient curves computed by different methods are nearly the same and are presented in Figure 8(a).

4.1.2. Results for $\alpha = 8°$

Table 3: NACA0012: Lift and drag coefficients for flow past a fixed NACA0012 airfoil at $\alpha = 8°$ and $Re = 3 \times 10^6$.

	Grid	p	Δt	C_L	C_D
IFEM (ChorinSAp1)	S1	1	0.00025	0.841	0.0143
IFEM (ChorinSAp2)	S1	2	0.00025	0.874	0.0149
IFEM (CoupledSAp1)	S1	1	0.00025	0.830	0.0141
IFEM (CoupledSAp2)	S1	2	0.00025	0.862	0.0144
IFEM (VMSp1)	S1	1	0.00025	0.871	0.0077
IFEM (VMSp2)	S1	2	0.00025	0.888	0.0124
Xfoil				0.897	0.0093
ANSYS Fluent (SA) [17]				0.812	0.0130
ANSYS Fluent ($k - \omega$ SST) [17]				0.791	0.0120
Exp: Abbott et al. [18]				0.887	0.0010

For $\alpha = 8°$ nothing special is observed except an increase in the lift coefficient. The exact values are shown in Table 3. Once again all the methods produce similar results. The VMS simulations using linear and quadratic spline elements compute values of lift coefficients which are closest to the experimental value. The slight tilt of the airfoil with respect to the incoming flow breaks the symmetry of the flow resulting in a relatively higher pressure caused by a sudden stagnation of the flow on the lower part of airfoil close to the leading edge (see Figures 9 and 10). For $\alpha = 0°$ the stagnation zone was just in front of the leading edge and was symmetric with respect to the centerline. The net imbalance in the vertical component of the pressure forces results in a lift force that is represented by the lift coefficient. The drag coefficient also shows a corresponding increase. The increase can be attributed to the larger obstruction offered at this angle of attack. The streamlines in Figures 11 and 12 confirm that although the flow is unsymmetric it is still attached to the airfoil surface. The pressure coefficient curves computed in different simulations even for this

Table 4: NACA0012: Lift and drag coefficients for flow past a fixed NACA0012 airfoil at $\alpha = 16°$ and $Re = 3 \times 10^6$.

	Grid	p	Δt	C_L	C_D
IFEM (ChorinSAp1)	S1	1	0.00025	1.008	0.1203
IFEM (ChorinSAp2)	S1	2	0.00025	1.462	0.0416
IFEM (CoupledSAp1)	S1	1	0.00025	1.010	0.1207
IFEM (CoupledSAp2)	S1	2	0.00025	1.461	0.0405
IFEM (VMSp1)	S1	1	0.00025	1.487	0.0663
IFEM (VMSp2)	S1	2	0.00025	1.546	0.0678
Xfoil				1.603	0.0220
ANSYS Fluent (SA) [17]				1.316	0.0320
ANSYS Fluent ($k - \omega$ SST) [17]				1.295	0.0280
Exp: Abbott et al. [18]				1.523	N/A

angle of attack are still exactly the same except close to the trailing edge where slight differences are observed, see Figure 8(b).

4.1.3. Results for $\alpha = 16°$

In the experimental results presented, the lift coefficient increases almost linearly up to an angle of attack $\alpha = 18°$ after which there is a sharp fall in the lift coefficient and a corresponding increase in the drag coefficient characteristic of the stalled condition. It is worth noting here that different methodologies (including those of others, i.e. Fluent) produce similar results up to an angle of attack of $\alpha = 15°$. However, at around an angle of attack of $\alpha = 16°$, the flow on the upper surface of the airfoil begins to separate and a condition known as stall begins to develop. At this point there are big variations in the prediction of lift coefficients by different simulations. The best predictions are by the VMS simulations. However, Table 4 reveals that almost all the simulations conducted with quadratic spline elements irrespective of the turbulence model do well to predict the lift coefficient accurately. In the current situation the effect of changing the order has little effect on the VMS simulations compared to that involving Spalart-Allmaras model. A closer inspection of Figures 11 and 12 reveals interesting facts regarding the flow behavior on the top surface. ChorinSAp1 predicts flow separation very close to the leading edge while in the CoupledSAp1 this is observed further downward. The VMSp1 predicts this separation further towards the trailing edge. An increase in the order of the elements suppresses the flow separation and makes it happen close to the trailing edge. The results predicted by ChorinSAp2, CoupledSAp2, VMSp1 and VMSp2 also compare well with the experiment. The fact that stall is not observed at $\alpha = 16°$ in the experiment also attests the fact that an increase in the order helps in predicting reality much better and hence their use is highly recommended.

4.1.4. Results for $\alpha = 20°$

An angle of attack $\alpha = 20°$ corresponds to a situation which is marked by flow separation predicted by all simulations. The difference is only in the location of the separation point. For the Spalart-Allmaras models this is closer to the leading edge compared to the VMS simulations. Table 5 shows that

the Spalart-Allmaras models make a better estimate of the lift coefficients with the best predictions by the one using quadratic elements. VMS simulations according to the Figures 9 - 12 are characterized by vortex shedding.

In general the flow behavior, pressure distribution, streamlines on the bottom side of the airfoil are very similar for all the methods adopted for a particular angle of attack. The profile of C_P, see Figure 8(d), stresses that point as the parts of all the profiles corresponding to the bottom surface nearly collapse into a single curve. However, on the part corresponding to the upper surface significant variations are observed especially for $\alpha = 16°, 20°$.

4.2. Comparison of the computational efficiency of different methods

Determination and comparison of the computational efficiency of the different methods is one of the main objectives of this work. All the simulations were conducted using our in-house CFD code IFEM. The linear solvers are based on the PETSc package [20] version 3.4.2 and are compiled with the Intel C++ compiler version 13.0.1, using the SGI MPT MPI implementation, all running on SUSE Linux Enterprise Server 11. The simulations were run on the "Vilje" supercomputer at the Norwegian University of Science and Technology which is currently ranked as number 99 on the top 500 list (June 2014). This is an SGI Altix system with Intel Xeon E5-2670 (Sandy Bridge) processors. The 1404 computational nodes in the system consists of 2 octa-core processors in SMP, with 20MB L3 cache per processor. The nodes are connected using a high-speed infiniband network.

To understand the computational behavior of the three methods evaluated in this work it is important to have a deeper understanding of how the solvers work. In a VMS-based solver, a single non-linear saddle-point system has to be solved at each time level without any additional equations. On the other hand, in a coupled Navier-Stokes solver in a RANS setting, an additional elliptic equation for eddy viscosity has to be solved along with the non-linear saddle-point system. The Chorin-based solver avoids the need to solve a non-linear saddle-point system at each time level, and rather updates the velocity and pressure through a series of elliptic solves. This is based on a hope that solving the elliptic equations will have a lower cost than solving a single saddle-point system. If used in a RANS setting, an additional equation is required to solve

Table 5: NACA0012: Lift and drag coefficients for flow past a fixed NACA0012 airfoil at $\alpha = 20°$ and $Re = 3 \times 10^6$.

	Grid	p	Δt	C_L	C_D
IFEM (ChorinSAp1)	S1	1	0.00025	0.723	0.2779
IFEM (ChorinSAp2)	S1	2	0.00025	0.849	0.2267
IFEM (CoupledSAp1)	S1	1	0.00025	0.726	0.2805
IFEM (CoupledSAp2)	S1	2	0.00025	0.845	0.2246
IFEM (VMSp1)	S1	1	0.00025	1.412	0.5060
IFEM (VMSp2)	S1	2	0.00025	1.345	0.2662
Xfoil				1.597	0.0658
ANSYS Fluent (SA) [17]				0.837	N/A
ANSYS Fluent ($k - \omega$ SST) [17]				1.125	N/A
Exp: Abbott et al. [18]				0.870	N/A

(a) ChorinSA   (b) CoupledSA   (c) VMS

(d) ChorinSA   (e) CoupledSA   (f) VMS

(g) ChorinSA   (h) CoupledSA   (i) VMS

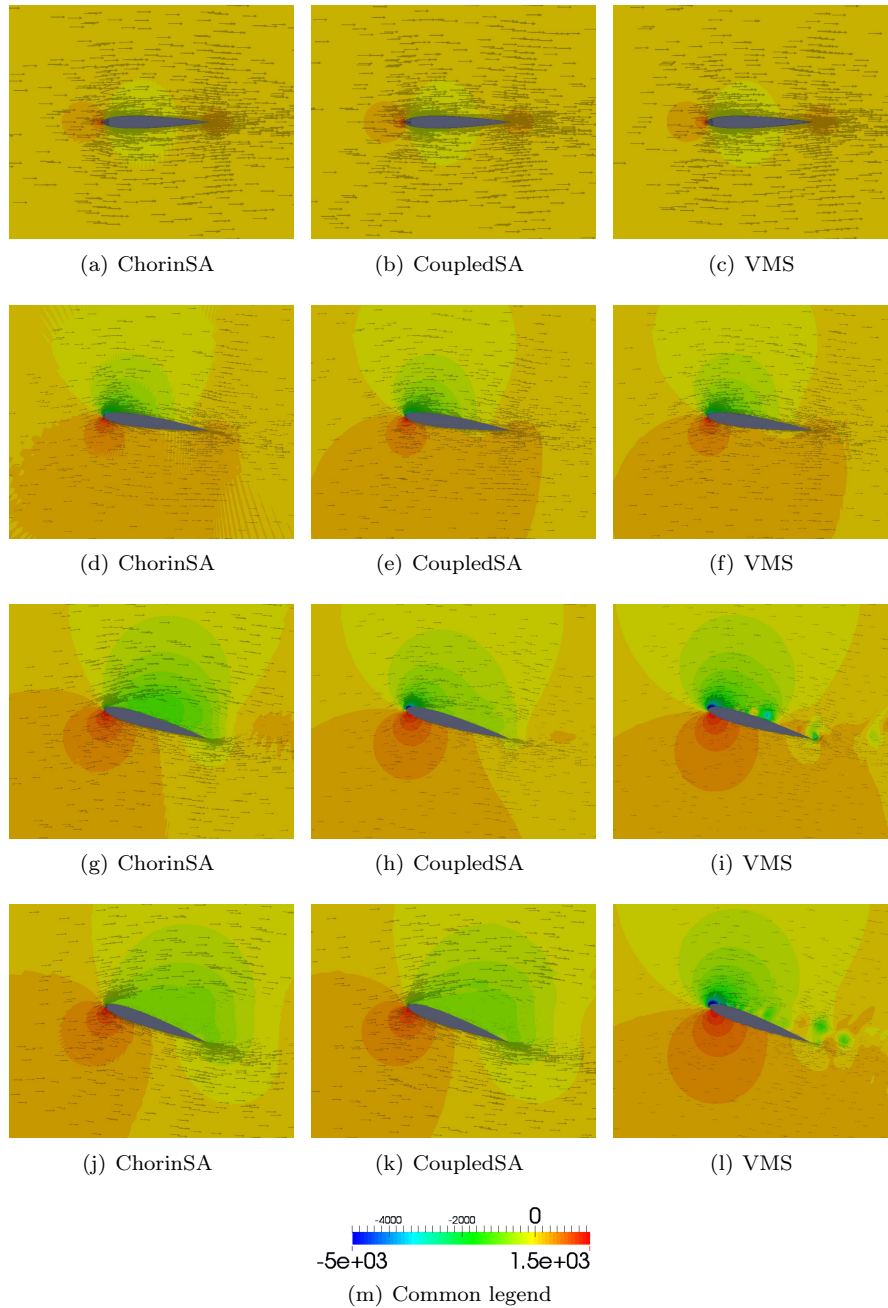(j) ChorinSA   (k) CoupledSA   (l) VMS

(m) Common legend

Figure 9: Pressure field computed by Chorin-SA, Coupled-SA, VMS for angles of attack of 0° (a-c), 8° (d-f), 16° (g-i) and 20° (j-l) with linear spline elements.
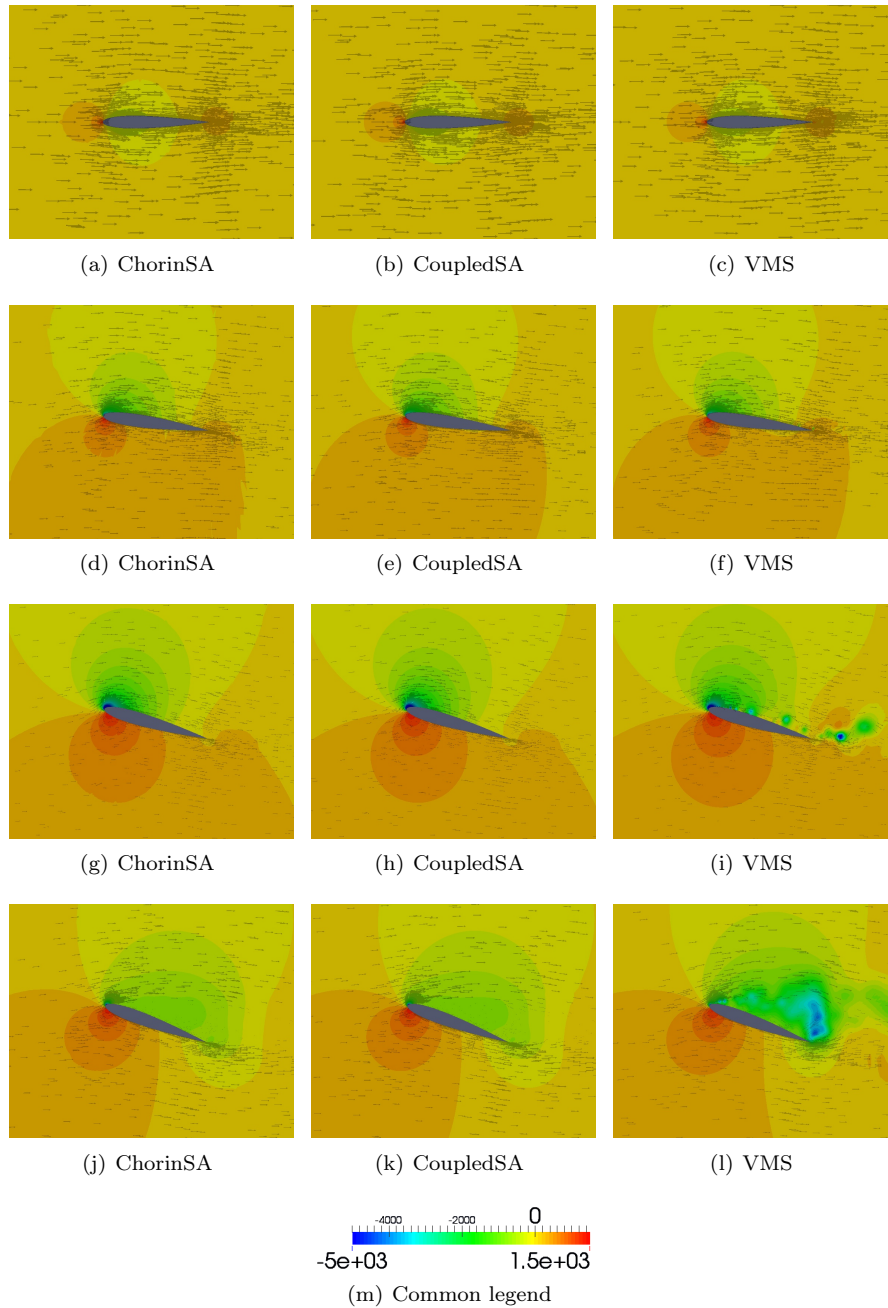
23

(a) ChorinSA   (b) CoupledSA   (c) VMS

(d) ChorinSA   (e) CoupledSA   (f) VMS

(g) ChorinSA   (h) CoupledSA   (i) VMS

(j) ChorinSA   (k) CoupledSA   (l) VMS

(m) Common legend

Figure 10: Pressure field computed by Chorin-SA, Coupled-SA, VMS for angles of attack of 0° (a-c), 8° (d-f), 16° (g-i) and 20° (j-l) with quadratic spline elements.
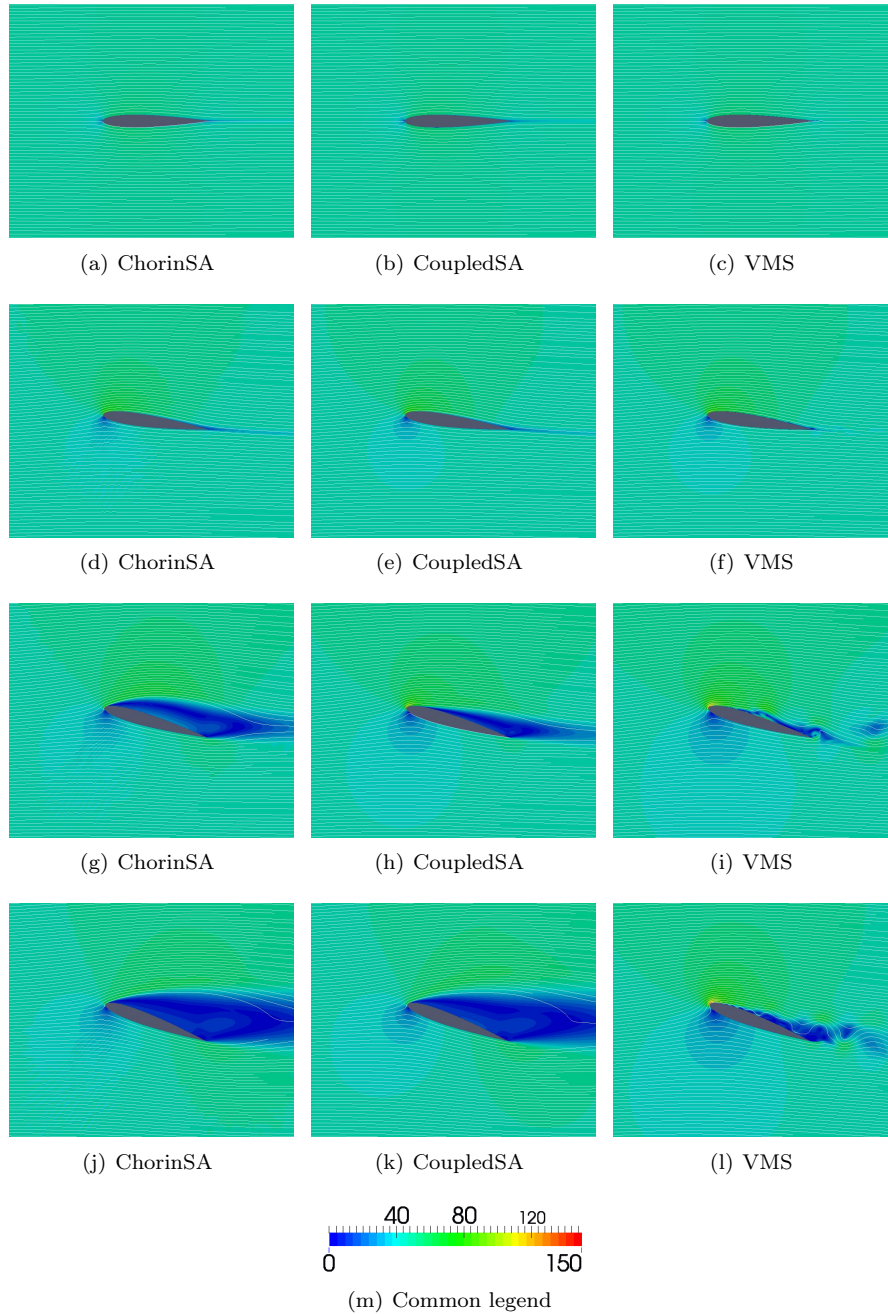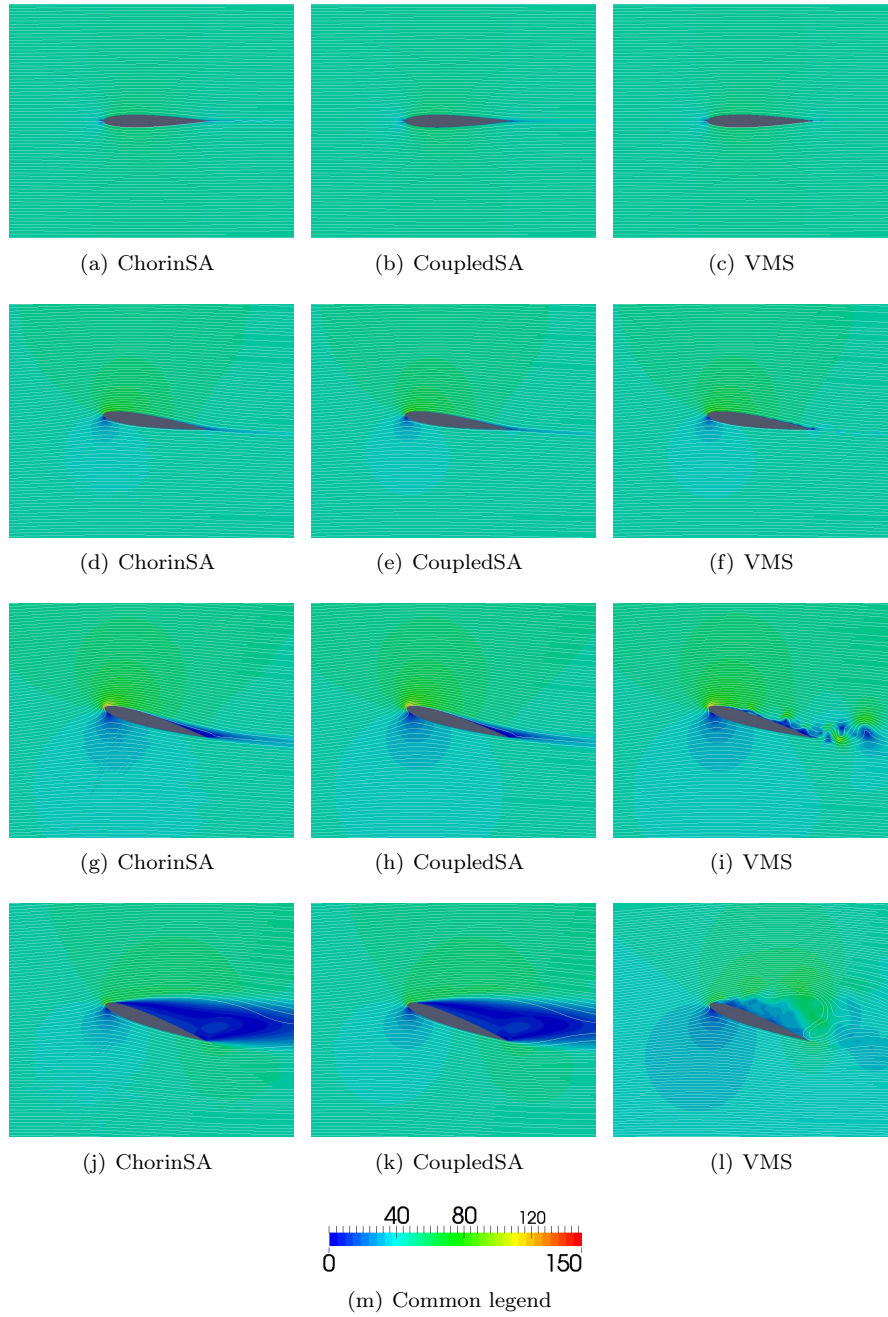
24

(a) ChorinSA   (b) CoupledSA   (c) VMS

(d) ChorinSA   (e) CoupledSA   (f) VMS

(g) ChorinSA   (h) CoupledSA   (i) VMS

(j) ChorinSA   (k) CoupledSA   (l) VMS

(m) Common legend

Figure 11: Velocity magnitude computed by Chorin-SA, Coupled-SA, VMS for angles of attack of 0° (a-c), 8° (d-f), 16° (g-i) and 20° (j-l) with linear spline elements.

25

(a) ChorinSA (b) CoupledSA (c) VMS

(d) ChorinSA (e) CoupledSA (f) VMS

(g) ChorinSA (h) CoupledSA (i) VMS

(j) ChorinSA (k) CoupledSA (l) VMS

(m) Common legend

Figure 12: Velocity magnitude computed by Chorin-SA, Coupled-SA, VMS for for angles of attack of 0° (a-c), 8° (d-f), 16° (g-i) and 20° (j-l) with quadratic spline elements.

for the eddy viscosity, giving a grand total of four elliptic solves per time step. It might now appear like the coupled solver in RANS setting will always be outperformed by the VMS-based solver, however this is not the case. The reason for this is the additional terms in Equation (13). These include the Hessian of the basis functions, which is expensive to evaluate (except for linears where it is zero by definition). Thus, for higher order elements the assembly time for the VMS approach will increase significantly. They also typically make the system matrix more ill-conditioned, resulting in a double penalty, as linear solves will increase in cost.

Furthermore, the use of isogeometric elements influences the results. The extra smoothness of the basis implies that there are basis functions with support across two elements, and which are smooth across the element boundaries. Since Gaussian quadrature is still used, and this can only be used with success if the integrand is smooth, more integration points are required per basis function. In particular, for quadratics one has to use two Gauss points per knot-span, where one classical element corresponds to two knot-spans (the support of a basis function). This results in more time being spent on assembly compared to traditional finite elements.

The total simulation time, calculated as an average of all 64 processors, is given in Figure 13. As expected, the difference in the total CPU time is more pronounced for simulations with $p = 2$ than for simulations with $p = 1$. For $p = 1$ the total CPU time is similar for all the three solvers. However, the VMS solver has a slight advantage, which is not a big surprise keeping in mind the discussion in the previous paragraph. The cost of solving and assembling extra systems is higher than the extra cost of assembling the VMS terms, since the Hessian can be skipped. For $p = 2$, however, the balance tips. Now the Chorin solver is significantly faster than the others, with the VMS solver as the slowest. This is the accumulated effect of the extra terms to be assembled, and the extra assembly caused by the isogeometric approach rearing its head. Additionally, the coupled approaches both are penalized at higher angles of attack. For the Chorin solver this does not seem to influence the simulation time to any significant degree.

In Figure 14 the ratio of CPU time spent on assembly compared to equation solving is given. We clearly see that this ratio drops for the coupled solvers for higher angles of attack, indicating that more time is spent on solving equations. Most likely, this is the effect of larger element aspect ratios in the boundary layer making the preconditioner less efficient. While this effect is also present for the Chorin solver, it is much less pronounced. This can be attributed to the SIMPLE approach used in the Schur-decomposition-based preconditioner for the saddle-point system. The multigrid sweep is a worse of the Helmholtz operator, and thus the pressure preconditioner block suffers. These results indicate that a RANS approach can be of great benefit for simulations with $p = 2$ or higher, in particular if a Chorin solver is employed. The figure shows clearly that the ratio is much higher for the VMS solver than the other solvers. For the high angles of attack the ratio is reduced both for the VMS and the coupled solver, which means that the solvers spend more time on equation solving.

The assembly process can be further analysed. For the coupled and VMS solver we normalize the CPU time by the average number of nonlinear iterations used in each time step. The result is shown in Figure 15. The huge difference between $p = 1$ and $p = 2$ is evident. For $p = 1$ the VMS solver spends the least
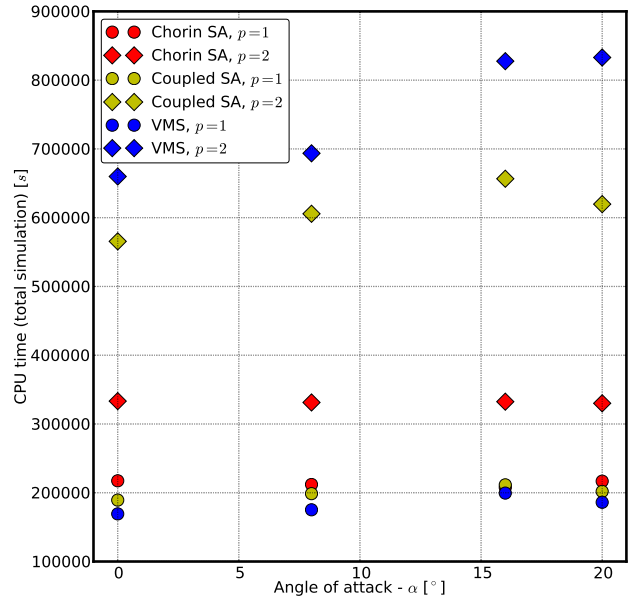
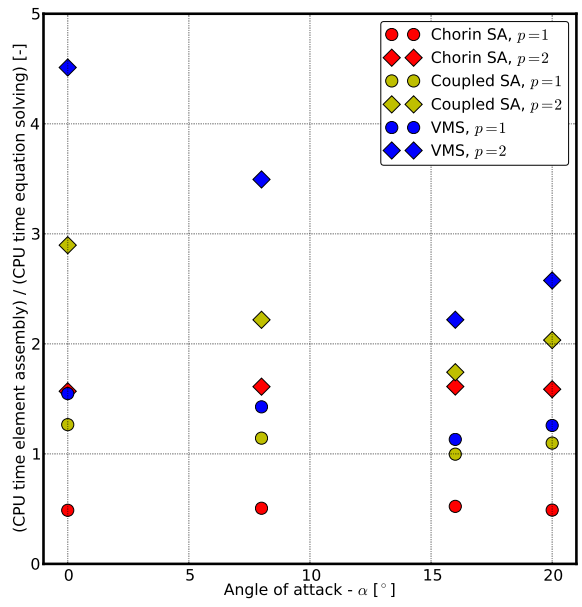Figure 13: NACA0012: Total CPU time for the simulations using all three solvers.

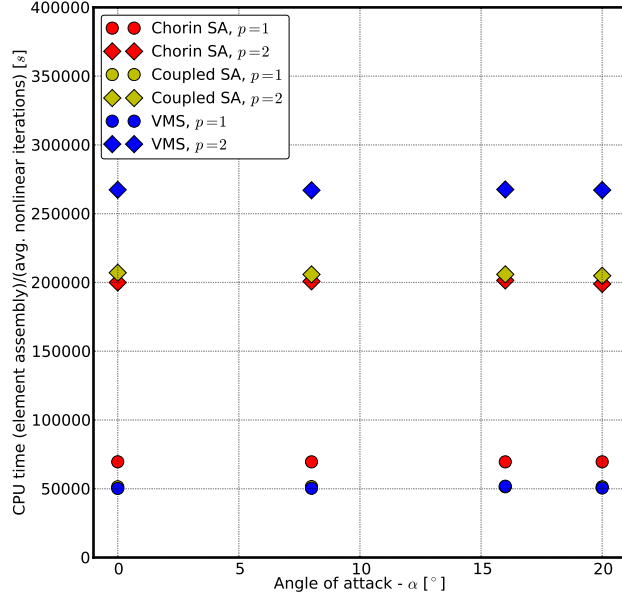Figure 14: NACA0012: Ratio of CPU time spent on element assembly and equation solving.

Figure 15: NACA0012: CPU time spent on element assembly (normalized by number of nonlinear iterations).

time of the three solvers on element assembly, but spends the longest time for $p = 2$.

5. Conclusions

In this work we have contributed a comparison of three isogeometric incompressible Navier-Stokes solvers. These three solvers are a Chorin solver with the Spalart-Allmaras turbulence model, a coupled Navier-Stokes solver with the Spalart-Allmaras turbulence model and a variational multiscale solver. All solvers have been used for investigating flows past a fixed NACA0012 airfoil at a Reynolds number 3×10^6 at four different angles of attack. The most significant findings are:

- computation of lift and drag coefficient in accordance with other references, both experimental and numerical. It seems to be relatively easy to predict lift and drag up to an angle of attack of $15°$ before which the flow is attached to the airfoil surface. Beyond an angle of attack of $15°$ we notice a large spread in lift and drag coefficients, meaning that it is more difficult to predict lift and drag when the flow enters the stall regime.

- increasing element order from 1 to 2 generally gives better approximation of lift, drag and pressure coefficients. However, the effect of increasing the element order from 1 to 2 is more pronounced for the Spalart-Allmaras models.

- there is not much difference between the total computational time for the three solvers with $p = 1$. With $p = 2$ the Chorin solver is significantly faster than the two others. The Chorin solver is not penalized at higher angles of attack in the same way as the other two solvers.

- a general recommendation for the kind of simulations presented in this paper, i.e. 2D simulation of high Reynolds number flow past an airfoil, is to use a RANS approach, preferably with a Chorin solver, with $p = 2$. The VMS solver would probably prove more useful if the goal is to investigate vortex shedding and wake effects. Furthermore, the conclusions presented herein apply to 2D simulations, separate investigations should be done for 3D simulations.

However, we want to underline that the VMS turbulence model is (theoretically only) applicable for three-dimensional flows. In this study we have suppressed the three-dimensionality of the flow thereby eliminating the physical processes like three-dimensional vorticity fluctuations and the associated vortex-stretching from happening. Thus, the simulation by VMS was reduced to a mere numerical exercise, and therefore not much should be read into their ability to model the physical processes. For this, separate three-dimensional studies should be undertaken. Having said that, the discussion regarding the computational efficiency still holds. One more point worth mentioning here is that for a RANS model like the Spalart-Allmaras model there is no need to run the simulations for so long because convergence is reached within approximately 1/4th of the total time of simulation we used. However, VMS owing to inherent unsteadiness had to be run for a much longer time to ensure statistical convergence. Thus the RANS simulations in this study are much faster than they appear in the paper.

References

[1] T. Hughes, J. Cottrell, Y. Bazilevs, Isogeometric analysis: CAD, finite elements, NURBS, exact geometry and mesh refinement, Comput. Methods Appl. Mech. Eng. 194 (39-41) (2005) 4135–4195.

[2] J. A. Cottrell, T. J. Hughes, Y. Bazilevs, Isogeometric analysis: toward integration of CAD and FEA, Wiley, Chichester, 2009.

[3] Y. Bazilevs, V. M. Calo, J. A. Cottrell, T. J. R. Hughes, A. Reali, G. Scovazzi, Variational multiscale residual-based turbulence modeling for large eddy simulation of incompressible flows, Comput. Methods Appl. Mech. Eng. 197 (2007) 173–201.

[4] V. M. Calo, Residual-based multiscale turbulence modeling: Finite volume simulation of bypass transistion, Ph.D. thesis, Stanford University (2004).

[5] I. Akkerman, Y. Bazilevs, V. Calo, T. Hughes, S. Hulshoff, The role of continuity in residual-based variational multiscale modeling of turbulence, Comput. Mech. 41 (3) (2008) 371–378.

[6] K. Valen-Sendstad, A. Logg, K.-A. Mardal, H. Narayanan, M. Mortensen, A Comparison of Some Common Finite Element Schemes for the Incompressible Navier-Stokes Equations, Vol. 84 of Lect. Notes Comput. Sci. Eng., Springer, 2012, Ch. 21, pp. 395–418.

[7] P. Spalart, S. Allmaras, One-equation turbulence model for aerodynamic flows, Recherche Aerospatiale 1 (1994) 5–21.

[8] S. R. Allmaras, F. T. Johnson, P. R. Spalart, Modifications and clarifications for the implementation of the Spalart-Allmaras turbulence model, in: 7th International Conference on Computational Fluid Dynamics (ICCFD7) Proceedings, 2012.

[9] F. Brezzi, L. P. Franca, T. J. R. Hughes, A. Russo, $b = \int g$., Comput. Methods in Appl. Mech. Engrg. 145 (1997) 329–339.

[10] T. J. R. Hughes, Multiscale phenomena: Green's functions, the Dirichlet-to-Neumann formulation, subgrid scale models, bubbles and the origins of stabilized methods, Comput. Methods Appl. Mech. Engrg. 127 (1995) 387–401.

[11] T. J. R. Hughes, G. R. Feijóo, L. Mazzei, J.-B. Quincy, The variational multiscale method – a paradigm for computational mechanics, Comput. Methods Appl. Mech. Engrg. 166 (1998) 3–24.

[12] T. J. R. Hughes, G. Sangalli, Variational multiscale analysis: the fine-scale Green's function, projection, optimization, localization, and stabilized methods, SIAM J. Numer. Anal. 245 (2007) 539–557.

[13] A. J. Chorin, Numerical solution of the Navier-Stokes equations, Math. Comp. 22 (1968) 745–762.

[14] R. Temam, Sur l'approximation de la solution des equations de navier-stokes par la methode des pas fractionnaires (ii), Arch. for Rational Mech. and Anal. 33 (5) (1969) 377–385.

[15] J. Guermond, P. Minev, J. Shen, An overview of projection methods for incompressible flows, Comput. Methods Appl. Mech. Eng. 195 (44-47) (2006) 6011–6045.

[16] L. Timmermans, P. Minev, F. Van De Vosse, An approximate projection scheme for incompressible flow using spectral elements, Int. J. for Numer. Meth. Fluids 22 (7) (1996) 673–688.

[17] D. C. Eleni, T. I. Athanasios, M. P. Dionissios, Evaluation of the turbulence models for the simulation of the flow over a National Advisory Committee for Aeronautics (NACA) 0012 airfoil, J. Mech. Eng. Res. 4 (3) (2012) 100–111.

[18] I. H. Abbott, A. E. von Doenhoff, Theory of wing sections, Dover Publishing, 1959.

[19] Xfoil.
URL http://web.mit.edu/drela/Public/web/xfoil/

[20] S. Balay, S. Abhyankar, M. F. Adams, J. Brown, P. Brune, K. Buschelman, V. Eijkhout, W. D. Gropp, D. Kaushik, M. G. Knepley, L. C. McInnes, K. Rupp, B. F. Smith, H. Zhang, PETSc Web page (2014).
URL http://www.mcs.anl.gov/petsc